





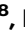


Unraveling the optoelectronic properties of CoSb_x intrinsic selective solar absorber towards high-temperature surfaces

Received: 15 December 2022

Accepted: 24 October 2023

Published online: 10 November 2023

 Check for updates

Anastasiia Taranova¹ , Kamran Akbar¹ , Khabib Yusupov², Shujie You³, Vincent Polewczyk⁴, Silvia Mauri^{4,5}, Eleonora Balliana⁶ , Johanna Rosen², Paolo Moras⁷, Alessandro Gradone⁸ , Vittorio Morandi⁸ , Elisa Moretti¹  & Alberto Vomiero^{1,3} 

The combination of the ability to absorb most of the solar radiation and simultaneously suppress infrared re-radiation allows selective solar absorbers (SSAs) to maximize solar energy to heat conversion, which is critical to several advanced applications. The intrinsic spectral selective materials are rare in nature and only a few demonstrated complete solar absorption. Typically, intrinsic materials exhibit high performances when integrated into complex multilayered solar absorber systems due to their limited spectral selectivity and solar absorption. In this study, we propose CoSb_x ($2 < x < 3$) as a new exceptionally efficient SSA. Here we demonstrate that the low bandgap nature of CoSb_x endows broadband solar absorption (0.96) over the solar spectral range and simultaneous low emissivity (0.18) in the mid-infrared region, resulting in a remarkable intrinsic spectral solar selectivity of 5.3. Under 1 sun illumination, the heat concentrates on the surface of the CoSb_x thin film, and an impressive temperature of 101.7 °C is reached, demonstrating the highest value among reported intrinsic SSAs. Furthermore, the CoSb_x was tested for solar water evaporation achieving an evaporation rate of 1.4 kg m⁻² h⁻¹. This study could expand the use of narrow bandgap semiconductors as efficient intrinsic SSAs with high surface temperatures in solar applications.

The high surface temperature under solar light illumination is highly beneficial for a wide range of applications such as steam generation, passive heating, thermoelectricity generation, anti-icing/deicing, catalysis, converting a control signal into mechanical motion, and solar water evaporation^{1–4}. Although surface temperature higher than 100 °C has been obtained under 1 sun illumination, this normally requires the

utilization of thermal insulation on top of the system to avoid heat losses⁵. This extra coverage on the top surface can restrict the penetrated light intensity due to its limited transparency and lead to condensation of generated vapors on the inner surface, commonly known as fogging. To overcome this drawback, various black absorber materials exhibiting broad solar absorption (0.3–2.5 μm) have been

¹Department of Molecular Sciences and Nanosystems, Ca' Foscari University of Venice, Via Torino 155, 30172 Venice, Italy. ²Department of Physics, Chemistry and Biology (IFM), Linköping University, 581 83 Linköping, Sweden. ³Division of Materials Science, Department of Engineering Sciences and Mathematics, Luleå University of Technology, SE-971 87 Luleå, Sweden. ⁴Istituto Officina dei Materiali (IOM) - CNR, Laboratorio TASC, Area Science Park, S.S. 14 Km 163.5, Trieste I-34149, Italy. ⁵Dipartimento di Fisica, University of Trieste, via A. Valerio 2, 34127 Trieste, Italy. ⁶Department of Environmental Sciences, Informatics and Statistics, Ca' Foscari University of Venice, Scientific Campus Via Torino 155/b, 30173 Venice, Italy. ⁷Istituto di Struttura della Materia (ISM) - CNR, S.S. 14 Km 163.5, Trieste I-34149, Italy. ⁸Istituto per la Microelettronica ed i Microsistemi (IMM) - CNR Sede di Bologna, via Gobetti 101, 40129 Bologna, Italy.

 e-mail: kamran.akbar@unive.it; ELISA.MORETTI@unive.it; alberto.vomiero@ltu.se

developed, such as carbon and polymeric-based materials, but their surface temperatures remain below 85 °C owing to excessive thermal re-radiation back to the environment in the mid-infrared (IR) region (2.5–20 μm)^{6,7}. This massive thermal re-radiation prevents heat concentration within the absorber and as a result, its surface temperature is drastically reduced. Following Kirchhoff's law of thermal radiation, for any material in thermal equilibrium, the ratio of the emissive power and the absorption coefficient is constant. This law has been applied to develop a promising class of materials called selective solar absorbers, for which a material with a low absorption coefficient in a specific spectral region will present low emission (and then low heat/energy dissipation) in the same region. SSAs are one of the classes of absorbers that can perfectly absorb the full-spectrum sunlight and avoid IR emission in the form of black body radiation, thanks to their low emission in the mid-IR region, avoiding thermal radiation heat losses. Hence, there is a dire need for materials possessing spectral selectivity with broad solar absorption ($\bar{\alpha}$) but simultaneous low mid-IR emission ($\bar{\epsilon}$) (see Supplementary Fig. 1). The ability of a surface to absorb the light in the desired wavelength, while simultaneously reflecting the undesired wavelength is called spectral selectivity, which can be defined as the ratio between the average absorptance and emittance $\bar{\alpha}/\bar{\epsilon}$.

Generally, in the reviews, SSAs surface coatings are classified into six categories depending on the structure and composition^{8–10}. The first type is intrinsic SSA with desired intrinsic selective properties. The intrinsic SSA is the simplest in configuration among other types, though the major drawback is the scarcity of intrinsic SSAs in nature. Some of the transition metals and semiconductors (e.g., TiO₂, MgF, SrF) exhibiting some intrinsic selectivity properties need to be improved for practical use^{11–15}. The second category includes composites of semiconductors and transition metals for attaining the desired spectral selectivity. In this combination, the low bandgap of the semiconductor is responsible for absorbing the short wavelengths, while the low emittance is provided by the metal layer⁸. The design of multilayer absorber solar selective coating consists of a substrate and multilayer dielectric (e.g., Al₂O₃, SiO₂, ZnS)/metal-metal oxide (e.g., Ag, Cu, Ni) combination and is based on the effect of multiple reflections between layers^{16,17}. The combination of a metal substrate and absorber possesses good light absorption characteristics, while extinction interference absorption increases the solar absorption for the interface between substrate and absorber. To enhance light absorption, a smoother transition of the optical constant from the absorber to air is needed, which is provided by the dielectric layer that covers the absorber^{18,19}. As multilayer solar selective coatings remain stable at a temperature above 400 °C, the further application can be attributed to the high-temperature range²⁰. Cermet-based solar absorbers are the incorporated metal particles in a dielectric or ceramic matrix²¹. Owing to their excellent optical properties—a high absorptance under solar irradiation and high reflectance in the IR region—cermets have been extensively investigated (e.g., Cr₂O₃, Al₂O₃, ZrO₂ based)^{22–24}. The selectively solar-transmitting coating on a blackbody-like absorber is commonly used for low-temperature applications (from ambient to 60 °C), while for high-temperature applications, the black absorber with highly doped semiconductors (e.g., SnO₂:Sb, In₂SO₃:Sn) has better performance^{25–27}. The last concept of achieving desired spectral selectivity refers to the surface texturing of material. Thus, metals with smooth polished surfaces exhibit low emissivity, while metals with rough surfaces possess undesirably high emissivity. Additionally, the emissivity also depends on the temperature of the surface as well as on incidence and wavelengths.

Other strategies for achieving low intrinsic mid-IR emissivity and full absorption in the sunlight spectral range include various light manipulation techniques such as the fabrication of metasurfaces, photonic crystals, etc.⁷. In a recent study, Li et al. reported intrinsically low mid-IR emissivity (down to 0.1) but high and broad solar absorptance (up to 0.9) of two-dimensional (2D) Ti₃C₂T_x MXenes thin films⁶.

As a result, the thin film attained a surface temperature of 89 °C under 1 sun illumination. However, standalone materials possessing simultaneously high solar absorption and low mid-IR emission are scarce, and only a few have been reported, such as HfC, ZrBr₂, CaF₂, SnO₂, and In₂O₃, and their intrinsic spectral selectivity is still far from satisfactory^{28–30}.

In this study, the intrinsic spectral selectivity of 5.3 of semiconductor CoSb_x (2 < x < 3, from this point forward, referred to as CoSb₃ from the main phase present in the sample) is demonstrated. Owing to its narrow bandgap of 0.26 eV, CoSb₃ exhibits a high and broad solar absorptance of 0.96 while its emissivity in the mid-IR region is only 0.18 at 100 °C. These are superior values compared to all intrinsic SSAs reported thus far. As a consequence, a thin film of CoSb₃ exhibits a record-high surface temperature of 101.7 °C among intrinsic SSA under 1 sun illumination. For proof of concept, the CoSb₃ was applied for solar water evaporation in a standard geometry using a glass fiber filter paper, which resulted in an evaporation rate of 1.4 kg m⁻² h⁻¹.

Results

Structural and morphology characterizations

The crystal structure of the CoSb₃ powder prepared by the solvothermal method (see “Methods” section) was investigated through different techniques. In X-ray Diffraction (XRD) measurements (see Supplementary Fig. 2a), the majority of the diffraction peaks confirmed the cubic skutterudite CoSb₃ phase (JCPDS #88–2437) of the *Im-3* space group. A second phase is also present, and the diffraction peaks at 32.34°, 32.26°, 33.96°, and 50.78° can be attributed to the (111), (−121), (210), and (131) crystallographic planes of the monoclinic structure of CoSb₂ (JCPDS #29–126). The crystalline structures of CoSb₃ and CoSb₂ are presented in Supplementary Fig. 2b, c, respectively. Mi et al. reported that the formation of the CoSb₃ phase by solvothermal synthesis is a typical heat-activated reaction that is limited by the maximum treatment temperature of the autoclave during the synthesis³¹. An alternative approach to obtain the CoSb₃ phase is to increase the treatment time of the autoclave inside the oven, allowing the formation of single phase CoSb₃ by increasing the synthesis temperature up to 250 °C, while at lower temperatures the secondary phase CoSb₂ is formed as an intermediate product. Both CoSb₃ and CoSb₂ phases coexist in our Co–Sb system and present channels or voids available for the diffusion of water molecules, which suggests the potential application of Co–Sb composites for solar steam generation. Based on the Scherrer equation (Supplementary Note 1), the average crystallite size *D* calculated from the strongest (013) reflection of the curve at 31.18° is 29.2 nm. From the Rietveld refinement analysis, the synthesized powder contains 72.8 wt.% CoSb₃ and 27.2 wt.% CoSb₂ (for details, see Supplementary Note 2).

Transmission Electron Microscopy (TEM) analysis (see Supplementary Fig. 3) gives the opportunity of a more detailed understanding of the system's structure. Supplementary Fig. 3a reports a TEM micrograph at low magnification of the cobalt antimonide sample where a particle-like shape with two different types of structures, enclosed in a μm-size aggregate is clearly shown in Fig. 1. The microstructure is composed of several particles with irregular shape, fused in larger structures or attached one to the other (blue dotted square) and a less concentrated secondary phase, with a rectangular shape (green dotted square). In Supplementary Fig. 3b, c are shown the high-resolution TEM (HRTEM) micrographs of the irregular particle, and of the one with rectangular shape, respectively. The former highlights the presence of several crystalline domains matching the one of CoSb₃ with a skutterudite cubic phase. The typical *d*-spacings of the skutterudite structure are highlighted in the FFT shown in the inset. The latter shows the presence of a different crystalline domain that corresponds to the one of a monoclinic CoSb₂ phase. The typical *d*-spacings of the monoclinic structure are highlighted in the FFT shown in

the inset. Finally, Supplementary Fig. 3d reports the selected area electron diffraction (SAED) pattern showing the typical behavior of a polycrystalline structure, due to the aggregation of many crystallites of different dimension and orientation. It is possible to recognize a polycrystalline pattern with the d -spacings of the cubic skutterudite phase (CoSb_3). It should also be noted the d -space value of 3.09 Å typical of a monoclinic phase CoSb_2 . These results are in perfect agreement with the results obtained by XRD. The high-angle annular dark field (HAADF) scanning transmission electron microscopy (STEM) micrograph of the cobalt antimonide sample helps in the visualization of the irregular (highlight with red arrows) and rectangular (highlight with yellow arrow) particles, embedded in the micrometric-size aggregate.

Supplementary Fig. 3e, f show the HAADF-STEM image of the cobalt-based aggregate, and the regions (points marked with 2 and 3) where the energy-dispersive X-ray spectroscopy (EDS) measurements

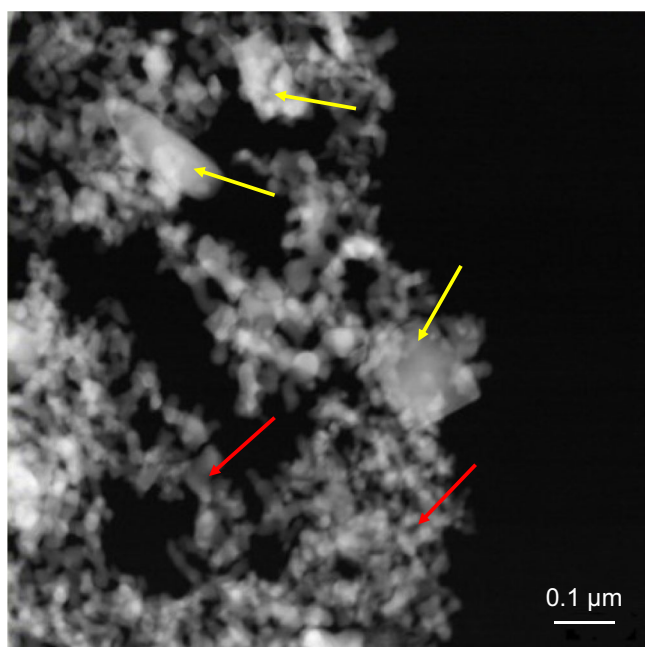


Fig. 1 | HAADF-STEM micrograph of CoSb_3 sample. The visualization of the irregular and rectangular particles, embedded in the micrometric-size aggregate, is highlighted with red and yellow arrows, respectively.

have been carried out and the resulting EDS spectra, respectively. The ratio in atomic percentage between Co and Sb changes, with a value of Co/Sb equal to 0.56 and 0.28 respectively for point 2 (rectangular particle) and point 3 (irregular particle), suggesting that the chemical composition and the shape are connected, in agreement with what observed by SAED and HRTEM analyses. The as obtained value perfectly match with the Co/Sb ratio respectively 0.5 of CoSb_2 and 0.33 of CoSb_3 . This last observation confirms the coexistence of two different phases in the system.

Supplementary Fig. 4a, b shows the surface morphology of CoSb_3 composed of grains of slightly irregular shape, with a particle size of 15–40 nm with some agglomerations, which confirms the XRD diffraction and the Scherrer calculation. The porosity of the nanosized particles, well visible from the scanning electron microscopy (SEM) images, may favor water diffusion within the mesoporous layer, which forms when the membrane is fabricated. The corresponding EDS elemental mapping of the CoSb_3 sample (see Supplementary Fig. 4c, d) reveals the uniform distribution of Co and Sb over the film and gives a Co:Sb atomic ratio of 1:2.83, close to the expected value of 1:3. From the cross-sectional image of Supplementary Fig. 4e, the thickness of the CoSb_3 absorber layer after being deposited on the membrane for functional tests is estimated to be ~35 μm. X-ray photoelectron spectroscopy (XPS) measurements, presented in Supplementary Fig. 5, show the presence of three different Sb-related compounds, i.e. CoSb_3 , CoSb_x ($x < 3$), and Sb_2O_3 at the extreme surface of the sample. The detailed XPS analysis is reported in Supplementary Note 3.

Optical measurements

Based on Fourier transform infrared (FTIR) data using the Tauc plot method presented in Fig. 2a it was established that CoSb_3 is a semiconductor with a direct band gap of ~0.26 eV³². This narrow bandgap allows interband electromagnetic radiation absorption to cover almost the entire solar spectrum. For this reason, CoSb_3 exhibits a high intrinsic absorbance ($\bar{\alpha}$) of 0.96 within the 0.3–2.3 μm wavelength spectral range (Fig. 2b), while simultaneously, the emissivity ($\bar{\epsilon}$) is only 0.18. Based on these values, the spectral selectivity ($\bar{\alpha}/\bar{\epsilon}$) of 5.3 is obtained, which is the highest value reported so far among intrinsic SSAs materials. The comparison between the current and reported record values is shown in Fig. 2c (see Supplementary Table 1).

Density functional theory (DFT) calculations

To assess the mechanism behind the intrinsic spectral selectivity of the prepared sample, the optical properties of CoSb_3 and CoSb_2 were

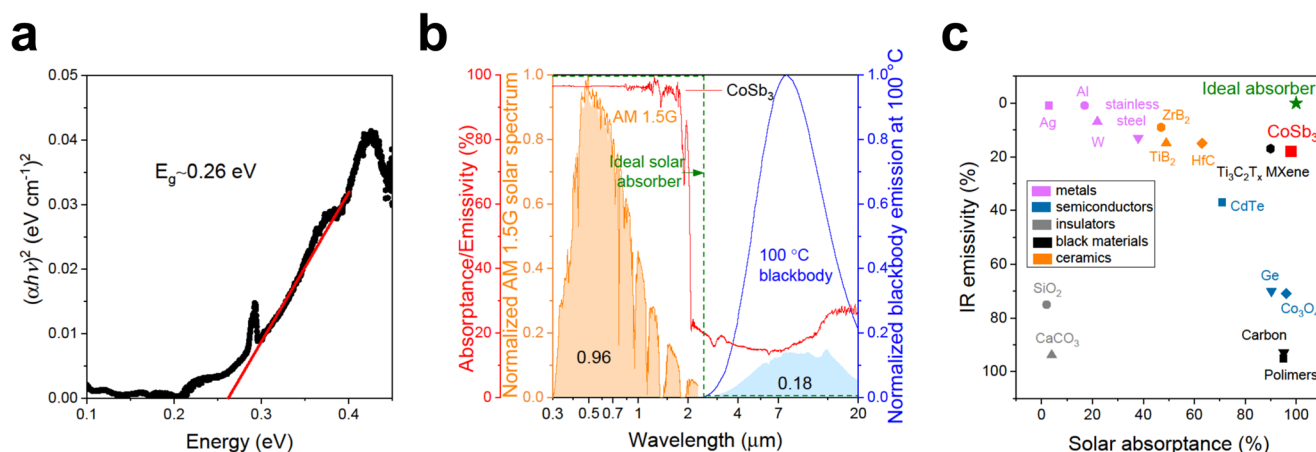


Fig. 2 | Optical properties of CoSb_3 . **a** Tauc plot and calculation of band gap energy E_g through the Tauc method. **b** Normalized absorbance/emissivity spectra of a CoSb_3 (red line), as well as the normalized AM 1.5G solar spectrum (orange) and the normalized radiation spectrum of a blackbody at 100 °C (blue). The spectrum of an ideal absorber (green line). The light blue area indicates the emissivity of the

present SSA, based on its experimentally measured absorbance. **c** Comparison of solar absorbance and IR emissivity of metals (Ag, Al, W, and stainless steel), radiative cooler materials (SiO_2 and CaCO_3), semiconductors (Ge, CdTe, and Co_3O_4), black materials (carbon-based and polymers), TiB_2 , ZrB_2 , HfC, and $\text{Ti}_3\text{C}_2\text{T}_x$ MXene.

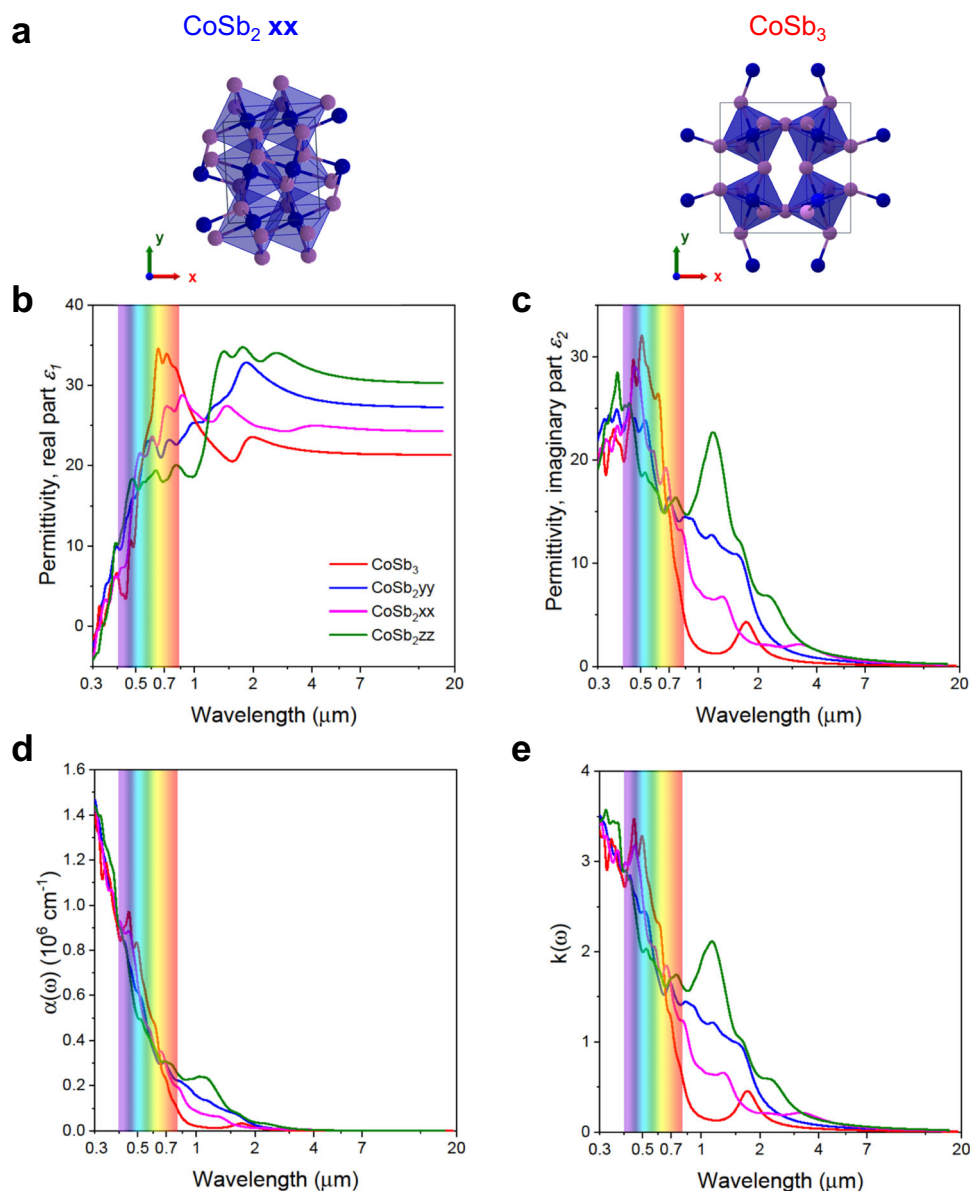


Fig. 3 | Calculated optical properties of CoSb₃. **a** Crystal structures of CoSb₂ and CoSb₃ in different directions (blue and purple balls represent Co and Sb

respectively). **b, c** Real (ϵ_1) and imaginary (ϵ_2) part of permittivity. **d** The absorption coefficient of CoSb₂ and CoSb₃. **e** The extinction coefficient of CoSb₂ and CoSb₃.

evaluated by the DFT calculations (see Supplementary Note 4). The presented theoretical results should be treated separately and cannot be directly compared to the obtained in the laboratory results. Theoretical findings are used to investigate the contribution of various phases on the optical properties and not to provide the absolute values. They were obtained for the case where the crystal structure is infinite, boundaries are absent and other restrictions affecting the obtained results. Real-world systems deviate from these idealized conditions, and theoretical results reflect a qualitative trend rather than specific values. The optical properties of CoSb₂ are directionally dependent owing to its monoclinic structure and thus different results were obtained in the *xx*, *yy*, and *zz* directions, see schematic in Fig. 3a, while for CoSb₃, due to its cubic symmetry, calculated data from different directions displayed similar results upon interaction with incident electromagnetic radiation. The corresponding permittivity data consisting of real (ϵ_1) and imaginary (ϵ_2) parts are displayed in Fig. 3b, c, respectively. The ϵ_1 can be equated to the resistance of the system to the external field, i.e., the creation of an internal field as a response to the external one. In the region from -0 to $-0.7 \mu\text{m}$ wavelength CoSb₃

exhibits growth of the permittivity (real part). Further on there is a decay, which is compensated by the directional behavior of CoSb₂ thus resulting in an almost constant built-in internal field. The ϵ_2 is associated with the absorption of the material, i.e., if the values are positive then the absorption is taking place. In the region from -0.7 to $-2.0 \mu\text{m}$ there is a sudden drop in ϵ_2 for CoSb₃, which results in drop of absorption for that material. However, it is compensated by the imaginary part of CoSb₂ hence keeping the ability of the material to exhibit strong absorptance in the region from 0 to $-2 \mu\text{m}$ wavelength, which supports the experimental results and explains the mechanism behind the performance. Beyond wavelength values larger than $2 \mu\text{m}$ (mid-IR region), the ϵ_2 drops for both CoSb₃ and CoSb₂ suggesting low mid-IR emissivity. However, ϵ_1 values in this region remain constant after the initial buildup of internal field. This, combined with the simultaneous low mid-IR emissivity in the IR region, leads to higher surface temperature.

Furthermore, the calculated absorption coefficients (Fig. 3d) for both CoSb₃ and CoSb₂ can explain the strong absorption in the UV-vis-NIR range up to $1 \mu\text{m}$ while minimal absorption is observed in the mid-

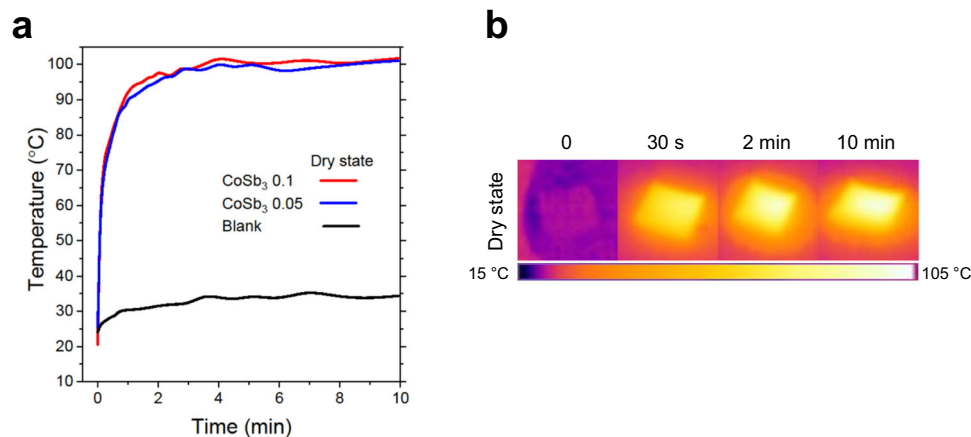


Fig. 4 | Surface temperature of CoSb₃ at dry state under 1 sun. a Photothermal behavior of wet CoSb₃ membrane under 1 sun illumination. **b** Time-lapse IR images of CoSb₃ 0.1 g membrane during water evaporation test.

IR region, strongly supporting the experimental observations. A similar trend has been observed for the extinction coefficient (Fig. 3e) of CoSb₃ and CoSb₂. Altogether, the DFT results indicate high absorption in UV-vis-NIR and low absorption in mid-IR. The optical features exhibited by CoSb₃ reproduce close to the optimal features for an ideal intrinsic SSA, i.e., very strong absorption within the 0.3–2.5 μm and almost negligible absorption for longer wavelengths. The calculated spectrum of transmittance and reflectance, normalized to unity, is shown in Supplementary Fig. 6a, b. From the reflectance spectrum the presence of CoSb₂ in the range 0.3–0.8 μm plays the dominant role in absorbing the incident light. The high theoretical reflectance values of around 0.5 and the high experimental average absorptance of 0.96 indicate that scattering is not negligible, and the secondary absorbance is taking place.

Solar test

To estimate the surface temperatures under 1 sun illumination, the photothermal response of the powders in the membrane was assessed with a calibrated IR camera, as shown in Fig. 4a, b. Experiments were conducted at an ambient temperature (23 ± 3) °C and relative humidity ~50%. To determine the effect of the thickness of the absorber, two membranes with 0.05 and 0.1 g of loaded powder were tested. The dried thin film on the glass fiber membrane was placed on a Styrofoam insulator substrate and illuminated with AM (air mass) 1.5 G (global) solar irradiation (100 mW cm⁻² irradiance). After 30 sec of illumination, the temperature on the surface of CoSb₃ 0.1 rises from 25 °C to 82.0 °C. In 10 min of illumination, a saturated surface temperature of 101.7 °C was recorded at equilibrium. Benchmarking experiment with a non-SSA (carbon cloth, see description in the “Methods” section) resulted in maximum surface temperature of 63 °C at 1 sun, reached after about 5 min of continuous illumination. It is worth mentioning that achievement of this high surface temperature with CoSb₃ is observed without additional modifications such as surface texturing, addition of antireflection coatings, etc. Most of the solar absorbers, which are presented in Supplementary Table 2, demonstrates high surface temperatures greater than 100 °C. However, it is attributed to the utilization of multilayered structures (where SSA is sandwiched between antireflection coating and materials with low IR emissivity such as metals), thermal insulation, surface texturing, metamaterials etc. In addition, to date only a handful of intrinsic SSAs have been discovered thus far and when tested standalone under one sun irradiations, their surface temperatures remain lower than what we have observed for CoSb_x thin films. The superior performance of 101.7 °C on the surface is the simultaneous combination of high intrinsic absorptance in the solar spectral region and low emissivity in the mid-IR region. High

intrinsic absorptance assures the maximum energy harvesting during irradiation, while simultaneous lower emissions in IR regions can suppress the heat loss to environment thus allowing heat concentration which ultimately leads to observed surface temperatures higher than 100 °C. The surface temperatures of CoSb₃ with 0.05 g loading of absorber material exhibit a saturation temperature of 100.9 °C, suggesting no effects from the thickness of the thin films. A blank test was performed to aid in the comparison. The result of the non-selective absorber confirms the role of low emissivity in the IR region for CoSb_x film to achieve high surface temperature.

During the solar vapor generation test (see Supplementary Fig. 7 and Supplementary Note 5), the equilibrium temperature for CoSb₃ 0.05 g and CoSb₃ 0.1 g reached 48.9 °C and 50 °C, respectively, after 10 min. The equilibrium temperature for the carbon cloth was 38.7 °C. The CoSb₃ samples exhibited evaporation rates of 1.3 and 1.4 kg m⁻² h⁻¹, respectively, which are three times higher than the evaporation rate of bulk water under 1 sun illumination. The benchmarking carbon cloth exhibited a steady state evaporation rate equal to 1.08 kg m⁻² h⁻¹, which is significantly lower than the one obtained through the proposed SSA. This experimental evidence confirms once again the critical role of selective absorption to reduce the radiative heat losses and to maximize the evaporation rate.

According to the wettability test (see Supplementary Fig. 7e), the photothermal CoSb₃ membrane exhibits hydrophilic properties as a drop of water with a volume of 5 μL was absorbed within 696 ms.

Water exhibits strong absorption in the IR region. For this reason, wet samples during solar water evaporation may lose their spectral selectivity. We investigated the optical absorption properties in the 2–20 μm spectral range on dry and wet CoSb_x, to give a semi-quantitative estimate of the worsening of selective absorption/emission properties of the sample in the wet condition, compared to the dry state. The results are reported in Supplementary Note 6 and Supplementary Fig. 8. As clearly visible, the presence of water worsens the selective absorption, as expected, in the spectral range 2–20 μm. Still, despite the increased absorptance, the sample exhibits a clear selective absorption/emission in the critical spectral region for solar water evaporation. Under wet condition, the surface temperature decreases. However, spectral selectivity still holds, and it leads to a high evaporation rate, as experimentally reported.

In summary, a narrow bandgap solar absorber CoSb₃ has been synthesized by the solvothermal method and has been demonstrated as an ideal candidate for efficient photothermal conversion and highly efficient solar vapor generation under 1 sun illumination. The surface temperature of the CoSb₃ membrane under 1 sun in the open air achieved ~101.7 °C. This superior value was achieved by optimal

intrinsic optical properties—high $\bar{\alpha}$ of 0.96 across the solar spectrum and low $\bar{\epsilon}$ of 0.18 in the mid-infrared region, achieving a record $\bar{\alpha}/\bar{\epsilon}$ of 5.3. The results represent one of the best performances among all intrinsic SSAs ever reported possibly caused by the presence of CoSb₂, potentially improving the optical properties. The comparison with a benchmarking non-selective absorber indicates the importance to limit radiative heat losses to obtain a high surface temperature. Furthermore, the thin CoSb₃ membrane showed a high rate of water evaporation of $\sim 1.4 \text{ kg m}^{-2} \text{ h}^{-1}$ under 1 sun illumination. The comparison with the benchmarking non-selective absorber shows that radiative emission in the IR region causes strong decrease of the evaporation rate, confirming that SSA is a viable strategy to obtain high evaporation rates. This study adds a new candidate to the existing small category of intrinsic SSA. The narrow bandgap and its association with high absorptance may open a field of research focused on narrow bandgap semiconductors possessing intrinsic broad solar absorptivity.

Methods

Synthesis

CoSb₃ was fabricated using the solvothermal synthesis. In a typical procedure, 3.6 mmol, 0.8213 g SbCl₃ ($\geq 99.0\%$, Sigma-Aldrich; UN Hazard Class: 8; UN Pack Group: II) and 1.2 mmol, 0.2855 g CoCl₂·6H₂O (98%, Sigma-Aldrich; Acute Tox. 4 Oral; Aquatic Acute 1; Aquatic Chronic 1; Carc. 1B Inhalation; Eye Dam. 1; Muta. 2; Repr. 1B; Resp. Sens. 1; Skin Sens. 1) were dissolved in a 120 mL ethanol bath. The solution was sonicated for 15 min, followed by the addition of 83.4 mol 0.4540 g NaBH₄ ($\geq 98.0\%$, Sigma-Aldrich; Acute Tox. 3 Oral; Eye Dam. 1; Repr. 1B; Skin Corr. 1B; Water-react 1) and sonicated for an additional 15 min for creating a reductive environment. Then the solution was sealed in a Teflon-lined stainless-steel autoclave with a 150 mL capacity and heated in an oven at 200 °C for 72 h. After cooling down to room temperature, the products were collected by centrifugation, washed using ethanol and deionized water several times, and dried at 70 °C overnight, isolated mass yields was estimated approximately 0.5 g.

The fabrication of the thin film membranes was performed through a vacuum filtration process. The powders with different masses of 0.05 and 0.1 g named CoSb₃ 0.05 and CoSb₃ 0.1, respectively, were dissolved in 250 mL of deionized water and then deposited on a glass microfiber filter paper with further drying.

Materials characterizations

The crystalline structure of the samples was obtained using XRD on a Philips PW1050/37 diffractometer. Additional details on crystal structure, nanoscale morphology, and composition were obtained with a FEI Tecnai F20 High-Resolution Transmission Electron Microscope, equipped with a Schottky transmitter operating at 200 kV. The elemental analysis was carried out by EDS, coupled with STEM-HAADF to map the elemental distribution. SEM images were acquired by using a scanning electron microscope Carl Zeiss AG-SUPRA 40 equipped with EDS, Oxford Instruments. XPS was performed to determine chemical compositions in a dedicated chamber of the NFFA UHV MBE-cluster system^{33,34}. The absorptance of the SSAs was measured using an ultraviolet-visible spectrophotometer LAMBDA 1050+, Perkin Elmer with an integrating sphere. A FTIR spectrometer (Nicolet 6700 FT-IR Spectrometer) equipped with a gold integrating sphere was used to record the IR spectrum of the compounds at room temperature.

The performance of a solar absorber can be evaluated by solar absorptance α and thermal emittance ϵ , which are calculated based on Kirchoff's law, spectrally averaged solar absorptance $\bar{\alpha}$, averaged thermal emissivity $\bar{\epsilon}$ are described in detail in Supplementary Note 7. The measurement of solar reflectance by standard spectrophotometers is limited by the 0.3–2.3 μm wavelength range at near-normal $\theta = 0^\circ$ angle of incidence.

The optical properties were calculated by the DFT using the hybrid Heyd–Scuseria–Ernzerhof (HSE) functional³⁵.

Solar steam generation test in lab

The rapid photothermal response of membranes under 1 sun without bulk water was recorded using a solar simulator Abet Technologies model 10500 with simulated solar flux at 1 sun, calibrated with a Si standard solar cell. IR images of the membranes under solar illumination were taken by an IR camera (FLIR C3-X). The temperature output of the IR camera was calibrated by using a hotplate and a thermocouple integrated into the hotplate. Details on the calibration procedure are reported in Supplementary Note 8 and in Supplementary Figs. 9 and 10. The dry temperature measurements were performed by placing the membranes onto thermal insulator surfaces such as Styrofoam under 1 sun illumination. The solar test and solar vapor generation test were described in Supplementary Note 9 and Supplementary Fig. 11.

For benchmarking purposes, we considered the photothermal and evaporation properties of a standard, non-selectively absorbing material to compare with the proposed SSA. We selected a carbon cloth (from Phychemi. www.phychemi.com, n. WOS1009), whose composition was carbon for more than 99.9% atomic. The choice of a commercial product was dictated to guarantee the highest possible reproducibility of our results at independent labs. We measured both the maximum temperature under dry condition and the evaporation rate under simulated solar flux at 1 sun. The measurement conditions and the experimental set-up were the same as the ones used for the SSA CoSb₃.

The wettability of the membrane was tested by the measurement of the contact angle using Phoenix 300 Touch (SEO, South Korea) and the software Surfaceware9.

Data availability

The authors declare that all data supporting the findings of this study are available within the article. The data generated in this study are provided in the Supplementary Information/Source data file. Source data are provided with this paper.

References

1. Fan, X. et al. A MXene-based hierarchical design enabling highly efficient and stable solar-water desalination with good salt resistance. *Adv. Funct. Mater.* **30**, 1–11 (2020).
2. Fan, X., Ding, Y., Liu, Y., Liang, J. & Chen, Y. Plasmonic Ti₃C₂T_x MXene enables highly efficient photothermal conversion for healable and transparent wearable device. *ACS Nano* **13**, 8124–8134 (2019).
3. Stranks, S. D. & Snaith, H. J. Metal-halide perovskites for photovoltaic and light-emitting devices. *Nat. Nanotechnol.* **10**, 391–402 (2015).
4. Zhou, L. et al. Self-assembled spectrum selective plasmonic absorbers with tunable bandwidth for solar energy conversion. *Nano Energy* **32**, 195–200 (2017).
5. Ni, G. et al. Steam generation under one sun enabled by a floating structure with thermal concentration. *Nat. Energy* **1**, 1–7 (2016).
6. Li, Y. et al. 2D Ti₃C₂T_x MXenes: visible black but infrared white materials. *Adv. Mater.* **33**, 2103054 (2021).
7. Li, Y., Lin, C., Huang, J., Chi, C. & Huang, B. Spectrally selective absorbers/emitters for solar steam generation and radiative cooling-enabled atmospheric water harvesting. *Glob. Chall.* **5**, 2000058 (2021).
8. Weinstein, L. A. et al. Concentrating solar power. *Chem. Rev.* **115**, 12797–12838 (2015).
9. Xu, K. et al. A review of high-temperature selective absorbing coatings for solar thermal applications. *J. Mater.* **6**, 167–182 (2020).
10. Zhang, J. et al. Solar selective absorber for emerging sustainable applications. *Adv. Energy Sustain. Res.* **3**, 2100195 (2022).
11. Pettit, R. B., Brinker, C. J. & Ashley, C. S. Sol-gel double-layer antireflection coatings for silicon solar cells. *Sol. Cells* **15**, 267–278 (1985).
12. Ning, Y. et al. NiCr–MgF₂ spectrally selective solar absorber with ultra-high solar absorptance and low thermal emittance. *Sol. Energy Mater. Sol. Cells* **206**, 110219 (2020).

13. Griffin, J. W., Stahl, K. A. & Pettit, R. B. Optical properties of solid particle receiver materials. I. Angular scattering and extinction characteristics of Norton Masterbeads®. *Sol. Energy Mater.* **14**, 395–416 (1986).
14. Ning, Y. et al. Tuning of reflectance transition position of Al-AlN cermet solar selective absorbing coating by simulating. *Infrared Phys. Technol.* **80**, 65–70 (2017).
15. Zheng, L. et al. Angular solar absorptance and thermal stability of Mo-SiO₂ double cermet solar selective absorber coating. *Sol. Energy* **115**, 341–346 (2015).
16. Schön, J. H., Binder, G. & Bucher, E. Performance and stability of some new high-temperature selective absorber systems based on metal/dielectric multilayers. *Sol. Energy Mater. Sol. Cells* **33**, 403–416 (1994).
17. El-Mahallawy, N., Atia, M. R. A., Khaled, A. & Shoeib, M. Design and simulation of different multilayer solar selective coatings for solar thermal applications. *Mater. Res. Express* **5**, 046402 (2018).
18. He, C. Y. et al. Toward high-temperature thermal tolerance in solar selective absorber coatings: choosing high entropy ceramic HfNbTaTiZrN. *J. Mater. Chem. A* **9**, 21270–21280 (2021).
19. He, C. Y., Zhao, P., Gao, X. H., Liu, G. & La, P. Q. Enhancing thermal robustness of a high-entropy nitride based solar selective absorber by the incorporation of Al element. *Mater. Today Phys.* **27**, 100836 (2022).
20. Zayed, M. E. et al. in *Sustainable Materials and Green Processing for Energy Conversion* 361–398 (Elsevier, 2022).
21. Zhang, Q. C. High efficiency Al-N cermet solar coatings with double cermet layer film structures. *J. Phys. D Appl. Phys.* **32**, 1938–1944 (1999).
22. Zhang, Q. C. & Mills, D. R. New cermet film structures with much improved selectivity for solar thermal applications. *Appl. Phys. Lett.* **60**, 545–547 (1992).
23. Ning, Y. et al. Optical simulation and preparation of novel Mo/ZrSiN/ZrSiON/SiO₂ solar selective absorbing coating. *Sol. Energy Mater. Sol. Cells* **167**, 178–183 (2017).
24. Cao, F. et al. Enhanced thermal stability of W-Ni-Al₂O₃ Cermet-based spectrally selective solar absorbers with tungsten infrared reflectors. *Adv. Energy Mater.* **5**, 1401042 (2015).
25. Granqvist, C. G. in *Physics and Technology of Solar Energy* 191–276 (Springer, 1987).
26. Kennedy, C. *Review of Mid-to High-Temperature Solar Selective Absorber Materials*. NREL Technical Report, 1–58 (National Technical Information Service, U.S. Department of Commerce, 2002).
27. Madhukeshwara, N. & Prakash, E. S. An investigation on the performance characteristics of solar flat plate collector with different selective surface coatings. *Int. J. Energy Environ.* **3**, 99–108 (2012).
28. Qiu, X. L., Gao, X. H. & Liu, G. Enhanced spectral selectivity of HfC based high temperature solar absorbers with the addition of Mo. *Thin Solid Films* **713**, 138349 (2020).
29. Gao, X. H., Qiu, X. L., Shen, Y. Q., He, C. Y. & Liu, G. A novel TiC-ZrB₂/ZrB₂/Al₂O₃ multilayer high temperature solar selective absorbing coating: microstructure, optical properties and failure mechanism. *Sol. Energy Mater. Sol. Cells* **203**, 110187 (2019).
30. Randich, E. & Allred, D. D. Chemically vapor-deposited ZrB₂ as a selective solar absorber. *Thin Solid Films* **83**, 393–398 (1981).
31. Mi, J. L., Zhao, X. B., Zhu, T. J., Tu, J. P. & Cao, G. S. Solvothermal synthesis and electrical transport properties of skutterudite CoSb₃. *J. Alloy. Compd.* **417**, 269–272 (2006).
32. Makuta, P., Pacia, M. & Macyk, W. How to correctly determine the band gap energy of modified semiconductor photocatalysts based on UV-Vis spectra. *J. Phys. Chem. Lett.* **9**, 6814–6817 (2018).
33. Torelli, P. et al. Experimental setup for high energy photoemission using synchrotron radiation. *Rev. Sci. Instrum.* **76**, 023909 (2005).
34. Vinai, G. et al. An integrated ultra-high vacuum apparatus for growth and in situ characterization of complex materials. *Rev. Sci. Instrum.* **91**, 085109 (2020).
35. Heyd, J., Scuseria, G. E. & Ernzerhof, M. Erratum: Hybrid functionals based on a screened Coulomb potential (*J. Chem. Phys.* **118**, 8207 (2003)). *J. Chem. Phys.* **124**, 219906 (2006).

Acknowledgements

A.V. acknowledges the Kempe Foundations, the Knut och Alice Wallenberg Foundation, the Luleå University of Technology (Labfund program) and the European Union - NextGenerationEU - through MUR (National Recovery and Resilience Plan (NRRP) – Mission 4 Component 2, Investment N. ECS00000043 – CUP N. H43C22000540006 (iNEST) and Mission 4 Component 2 Investment 1.3 - CUP D43C22003090001 (NEST)). This work has been carried out within the agreement “Convenzione operativa per collaborazione scientifica tra CNR ISM e Dipartimento di Scienze Molecolari e Nanosistemi Università Cà Foscari Venezia (Prot.n. 709, 14/04/2021).” Partial support through the project EUROFEL-ROADMAP ESFRI is gratefully acknowledged. J.R. acknowledges funding from the Göran Gustafsson foundation. The calculations were carried out using supercomputer resources provided by the Swedish National Infrastructure for Computing (SNIC), partially funded by the Swedish Research Council through grant agreement no. 2018-05973. This work has been partially performed in the framework of the Nanoscience Foundry and Fine Analysis (NFFA-MUR Italy Progetti Internazionali) facility (<https://www.trieste.nffa.eu/>). A.G. and V.M. acknowledge funding from the European Commission projects Graphene Flagship Core3, grant agreement No 881603, CHALLENGES, grant agreement No 861857, and from the European Union - NextGenerationEU under the National Recovery and Resilience Plan (NRRP), Mission 04 Component 2 Investment 3.1, Project Code: IR0000027 - CUP: B33C22000710006 - iENTRANCE@ENL: Infrastructure for Energy TRAnstition aNd Circular Economy @ EuroNanoLab

Author contributions

A.T., K.A., E.M., and A.V. conceived the idea and designed the experiments. A.T., S.Y., K.A., and E.B. performed investigation on optical properties and solar water evaporation test. V.P., S.M., and P.M. performed the X-ray photoelectron spectroscopy measurements and data analysis. A.G. and V.M. performed HRTEM (EDS) and STEM-HAADF measurements and data analysis. K.Y. and J.R. conducted the density functional theory calculations and data analysis. A.T., K.A., and A.V. wrote the paper with contributions from all authors.

Funding

Open access funding provided by Lulea University of Technology.

Competing interests

The authors declare no competing interests.

Additional information

Supplementary information The online version contains supplementary material available at <https://doi.org/10.1038/s41467-023-42839-6>.

Correspondence and requests for materials should be addressed to Kamran Akbar, Elisa Moretti or Alberto Vomiero.

Peer review information *Nature Communications* thanks Xiang-Hu Gao and the other, anonymous, reviewer for their contribution to the peer review of this work. A peer review file is available.

Reprints and permissions information is available at <http://www.nature.com/reprints>

Publisher's note Springer Nature remains neutral with regard to jurisdictional claims in published maps and institutional affiliations.

Open Access This article is licensed under a Creative Commons Attribution 4.0 International License, which permits use, sharing, adaptation, distribution and reproduction in any medium or format, as long as you give appropriate credit to the original author(s) and the source, provide a link to the Creative Commons licence, and indicate if changes were made. The images or other third party material in this article are included in the article's Creative Commons licence, unless indicated otherwise in a credit line to the material. If material is not included in the article's Creative Commons licence and your intended use is not permitted by statutory regulation or exceeds the permitted use, you will need to obtain permission directly from the copyright holder. To view a copy of this licence, visit <http://creativecommons.org/licenses/by/4.0/>.

© The Author(s) 2023, corrected publication 2024